

Article

2D Nanostructured MXene-Based Silver Nanoparticles for Photocatalytic Degradation of Safranin Dye

Muhammad Faheem ¹, Asim Riaz ², Manawwer Alam ³ , Faiza Wahad ¹ , Manzar Sohail ⁴, Muhammad Altaf ^{1,*} 
and Syed Mustansar Abbas ^{5,*}

¹ Department of Chemistry, Government College University, Lahore 54000, Pakistan; faizawahad@outlook.com (F.W.)

² Research School of Engineering, The Australian National University, Canberra, ACT 2601, Australia

³ Department of Chemistry, College of Science, King Saud University, Riyadh 11451, Saudi Arabia; maalam@ksu.edu.sa

⁴ Department of Chemistry, School of Natural Sciences, National University of Science and Technology, Islamabad 44000, Pakistan; manzar.sohail@sns.nust.edu.pk

⁵ Nanoscience and Technology Department, National Centre for Physics, Islamabad 45320, Pakistan

* Correspondence: muhammad.altaf@gcu.edu.pk (M.A.); mustansar.abbas@ncp.edu.pk (S.M.A.)

Abstract: Due to their unique chemical structure, MXenes have been recognized as a potential material, having a high surface area, high thermal and electrical conductivity, and a tunable band gap, showing great hydrophilicity and stability. The adsorption and reducing properties of MXene-based 2D nanomaterials make them efficient photocatalysts for degrading organic pollutants. Silver nanoparticles were synthesized over the exfoliated MXene sheets (1:50 and 1:20 by weight to silver salt) using polyvinyl pyrrolidone as a dispersant. The elemental composition and morphology of the nanocatalysts Ag₂₀@Ti₃C₂T_x and Ag₅₀@Ti₃C₂T_x were analyzed by X-ray diffraction (XRD) analysis, X-ray photoelectron spectroscopy (XPS), energy-dispersive X-ray (EDX) spectroscopy, and field-emission scanning electron microscopy (FESEM). FESEM micrographs reveal porous exfoliated Ti₃C₂T_x sheets obtained by continuously stirring Ti₃AlC₂ for 44 h at 60 °C, providing a platform for the growth of Ag nanoparticles. Diffused reflectance spectroscopy (DRS) indicates that the bare silver nanoparticles show a decrease in the band gap value from 2.4 to 1.35 and 1.41 eV in Ag₅₀@Ti₃C₂T_x and Ag₂₀@Ti₃C₂T_x, respectively, which enables the nanocomposites to show excellent catalytic performance and degrade around 99% of safranin dye within 15 min at a concentration of 5 mg Ag₅₀@Ti₃C₂T_x.

Keywords: 2D MXene; Safranin dye; nanocatalyst; band gap



Citation: Faheem, M.; Riaz, A.; Alam, M.; Wahad, F.; Sohail, M.; Altaf, M.; Abbas, S.M. 2D Nanostructured MXene-Based Silver Nanoparticles for Photocatalytic Degradation of Safranin Dye. *Catalysts* **2024**, *14*, 201. <https://doi.org/10.3390/catal14030201>

Academic Editor: Jorge Bedia

Received: 10 January 2024

Revised: 14 February 2024

Accepted: 17 February 2024

Published: 19 March 2024



Copyright: © 2024 by the authors. Licensee MDPI, Basel, Switzerland. This article is an open access article distributed under the terms and conditions of the Creative Commons Attribution (CC BY) license (<https://creativecommons.org/licenses/by/4.0/>).

1. Introduction

MXene (2D titanium carbide) is a promising candidate with many applications due to its high conductivity, inherent structural stability, high hydrophilicity, high tribological characteristics, excellent thermal conductivity, tunable band gap, and functionalization characteristics [1–3]. MXene is expressed by the general formula M_{n+1}X_nT_x (n = 1 to 3), where “M” is the respective transition metal, “X” can be the carbon atom or nitrogen atom joined by hydrogen bonding or Van der Waals interactions, while T_x represents the corresponding surface functionality, i.e., F[−], O[−], OH[−] [4–6]. The hydrophilic functionalities provide active sites on the surface of sheets and enable the structure to interact with the other functional groups. In contrast to other carbon-based materials (graphene, carbon nanotube), MXene materials exhibit a high reduction capacity [7–9]. The unique 2D structure of MXene-coupled hybrid materials with robust redox ability and anisotropic charge transfer performance make it high-potential material that is widely used as an electrocatalytic sensor material and photocatalyst for the degradation of pollutants present in the environment [10–13].

Ti₃C₂-based MXene possesses terminal metals exposed to the other functionalities and has high redox properties which helps in the degradation of hazardous environmental organic pollutants. The photocatalytic application of Ti₃C₂T_x has been widely studied due to its narrow tunable band gap ranges between 0.92 and 1.75 eV [14–16]. Density functional theory (DFT) calculations reveal that Ti₃C₂ exhibits metallic conductivity with a Fermi level value of -0.05 V. This is more positive than the conduction band of most n-type semiconductors, indicating the potential of Ti₃C₂ as a co-catalyst for the transfer and assembly of photogenerated electrons [17]. The absorption of visible light results in the production of photogenerated electrons that are excited from the valence band (VB) to the conduction band (CB), leaving holes in the valence band. The transfer of these excited charge carriers coupled with the co-catalyst is accelerated by the presence of Ti₃C₂-derived 2D carbon layers. Electrons transferred to MXenes are trapped in the sheets and generate H₂ by reducing H⁺ [18], CO, and CH₄ by reducing CO₂ [19], or NH₃ by reducing N₂ [20]. On the other hand, the transfer of holes to MXenes results in the production of OH[•] radicals, which could carry out organic degradation, while OH[•] radicals can also be produced through electrons for organic degradation [4].

The rapid industrialization has resulted in excessive hazardous wastes, including organic pollutants such as antioxidants, benzenes, tetracycline hydrochlorides, and sulfonamides [21], industrial dyes including cationic dyes (methylene blue, rhodamine B [22,23], crystal violet, safranin, malachite green, neutral red), anionic dyes (Congo red, methyl orange, and Eriochrome black T, acid red 1, acid blue 80 [6]), antibiotics (such as sulfadiazine SMZ, erythromycin, azithromycin, tetracycline [24], penicillin, chloramphenicol, rifampicin, ciprofloxacin) and carbamazepine used in the medical industry [25], bisphenol A [26,27], and many pesticides used in agriculture. These toxic substances, especially the persistent organic pollutants (POP) such as dioxin, oxole, chlordane, and dichlorodiphenyltrichloroethane, are a serious threat to the global environment affecting both terrestrial and aquatic life [10]. These environmental effects lead to the significant need for organic pollution degradation strategies to treat wastewater to remove these hazardous substances [11]. Air, soil, wastewater, river water, etc., can be decontaminated by converting the toxic organic compounds to environmentally friendly byproducts. The methods for eliminating organic pollutants include electrochemical conversion/combustion, chemical oxidation, biodegradation, etc. However, the abovementioned methods cannot remove low-level harmful organic pollutants, which may result in secondary pollutants too. To remove these harmful organic pollutants, a new type of advanced oxidation technology needs to be developed that is low-cost, high-efficiency, and environmentally friendly. Hence, photocatalytic degradation technology is an efficient solution for the degradation of these harmful toxic pollutants. Amid different kinds of photocatalysts, MXene, being a semiconductor material, possesses a tunable bandgap and has gained practical applications in the photocatalytic degradation of organic pollutants.

In comparison to other carbonaceous materials (like graphene and carbon nanotubes), the large surface area, high hydrophilicity, and functionalized (OH⁻, F⁻) accordion-like structure of MXene enable the sheets to reduce organic as well as inorganic pollutants and convert them to less toxic forms [10,11]. Fluoride-based etching of Ti₃AlC₂ results in the appearance of negative surface charges (F⁻, O⁻, and OH⁻ functional groups). However, a positive charge is more likely to appear on the metal atom due to incomplete bonding at the outer edges. The appearance of charge on the surface of the MXene sheet is also pH-dependent. At a low pH, the edges remain positively charged and are rarely affected by protons, while the negative terminal functionality such as O⁻ accepts a proton to form hydroxyl ions and eventually maintain negative charges. In contrast, a high pH leads to the neutralization of OH⁻ by the positively charged Ti atoms. The self-reduction properties of MXene facilitate the growth of silver (Ag) nanoparticles on exfoliated Ti₃C₂T_x sheets. Moreover, Ti₃C₂-based MXene exhibits a negative charge with a zeta potential of -30 mV at pH 7.0, which shows that these materials are susceptible to fabricating the metal ions on its surface [28].

Silver nanoparticles deposited on MXene show efficient photocatalytic and electrocatalytic activity due to the charge transfer mechanism [29]. However, the effect of MXene concentration on the synthesis of silver nanoparticles on a large scale, on exfoliated MXene sheets, with a tremendous decrease in the band gap was still unclear and worth exploring. The band gap of silver nanoparticles by the addition of MXene sheets makes the composite an efficient photocatalyst [13]. To investigate the reducing nature of MXene, two different concentrations (i.e., 1:20 and 1:50 wt % MXene to AgNO_3) were synthesized in the present study. The nanocomposite with 1:20 wt % MXene shows excellent photocatalytic activity for the degradation of safranin dye. This efficient strategy provides a basis for the fabrication of nanoparticles used for photocatalysis.

2. Results and Discussion

XRD analysis of pristine Ti_3AlC_2 exhibits the diffraction peaks at 2θ of 9.50° , 19.19° , 34.08° , 38.81° , 41.79° , 48.49° , 52.32° , 56.42° , 60.29° , 65.5° , 70.3° , and 73.8° , indexed to (002), (004), (101), (103), (104), (105), (107), (108), (109), (110), (201), and (202) planes that correspond to the crystal structure of the Ti_3AlC_2 MAX phase matching with the JCPDS card 98-010-5483 [15]. The XRD pattern of exfoliated Ti_3AlC_2 is given in Figure 1a, showing characteristic peaks at 5.98° , 9.11° , 18.22° , 27.65° , 35.99° , 41.89° , and 60.63° , which correspond to (002), (004), (101), (103), (105), and (110) planes of $\text{Ti}_3\text{C}_2\text{T}_x$. During the etching of aluminum metal, the peaks at 9.50° and 19.19° shifted the (002) and (004) planes slightly to a lower 2θ with a decrease in the peak intensity owing to the loss of the crystalline nature of the MAX phase. The strength of the peak at 9.50° 2θ did not change but decreased significantly in intensity because of the appearance of F^- and OH^- groups, which were further confirmed by XPS. However, the peak intensity of characteristic planes (103), (104), and (105) decreased more prominently along with the broadened (002) plane [16]. The characteristic peak at 38.81° decreased with the appearance of a peak at 27.65° , depicting the etching of Ti_3AlC_2 and conversion into the MXene phase. No representative peaks of AlF_3 were present at 25.3° , 35.2° , 43.5° , 52.1° , and 57.3° (JCPDS card no 750450) in $\text{Ti}_3\text{C}_2\text{T}_x$ which was further confirmed by EDX and XPS analyses [17].

In addition, three diffraction peaks appeared in the XRD pattern of $\text{Ag}_{20}\text{@Ti}_3\text{C}_2\text{T}_x$ and $\text{Ag}_{50}\text{@Ti}_3\text{C}_2\text{T}_x$ at 38.21° , 44.41° , 64.63° , and 77.43° 2θ , with planes (111), (200), (220), and (311), respectively, as shown in Figure 1b. This represents the cubic, single silver crystals [13]. The sharpness of the peaks depends upon the crystal structure of silver and the amount embedded in the MXene substrate. Due to the presence of the high loading of silver on the surface of MXene, the peak due to the (108) plane of MXene shows a relatively small intensity.

The surface elemental valance composition of Ti_3AlC_2 , $\text{Ti}_3\text{C}_2\text{T}_x$, and $\text{Ag}_{50}\text{@Ti}_3\text{C}_2\text{T}_x$ were analyzed by XPS, as shown in Figure 2. The survey spectrum presents the presence of the required elements in the form of Ag, Ti, O, and C, along with a small amount of fluorine coming from the etchant. By comparing the full-range (200–1200 eV) XPS spectrum of the pristine MAX phase, exfoliated MXene, and MXene-silver nanocomposites, the Ti 2p region consists of three asymmetric doublets at 455.1, 458.5, and 464 eV that were attributed to Ti (II) ($2p_{1/2}$), Ti (III) ($2p_{3/2}$), and Ti (III) ($2p_{1/2}$), respectively (Figure 3a). These peaks correspond to the MXene structure where C–Ti–C is the core layer, and the bonding of C–Ti–X, (X = F, O, OH) corresponds to the bonding of Ti atoms to the C-atom and terminal group [18,30]. The peak at 456.8 eV represents the Ti (II) to Ti (III) oxidation of titanium, and Ti (IV) $2p_{3/2}$ peak (~457 eV) correspond to titanium oxide (TiO_2) formation. However, the peak appearing at 460.6 eV is labelled as TiF_3 , resulting from the etching process of HF. The low-valent distinctive Ti species are responsible for the deposition of metallic silver on the MXene surface [30,31].

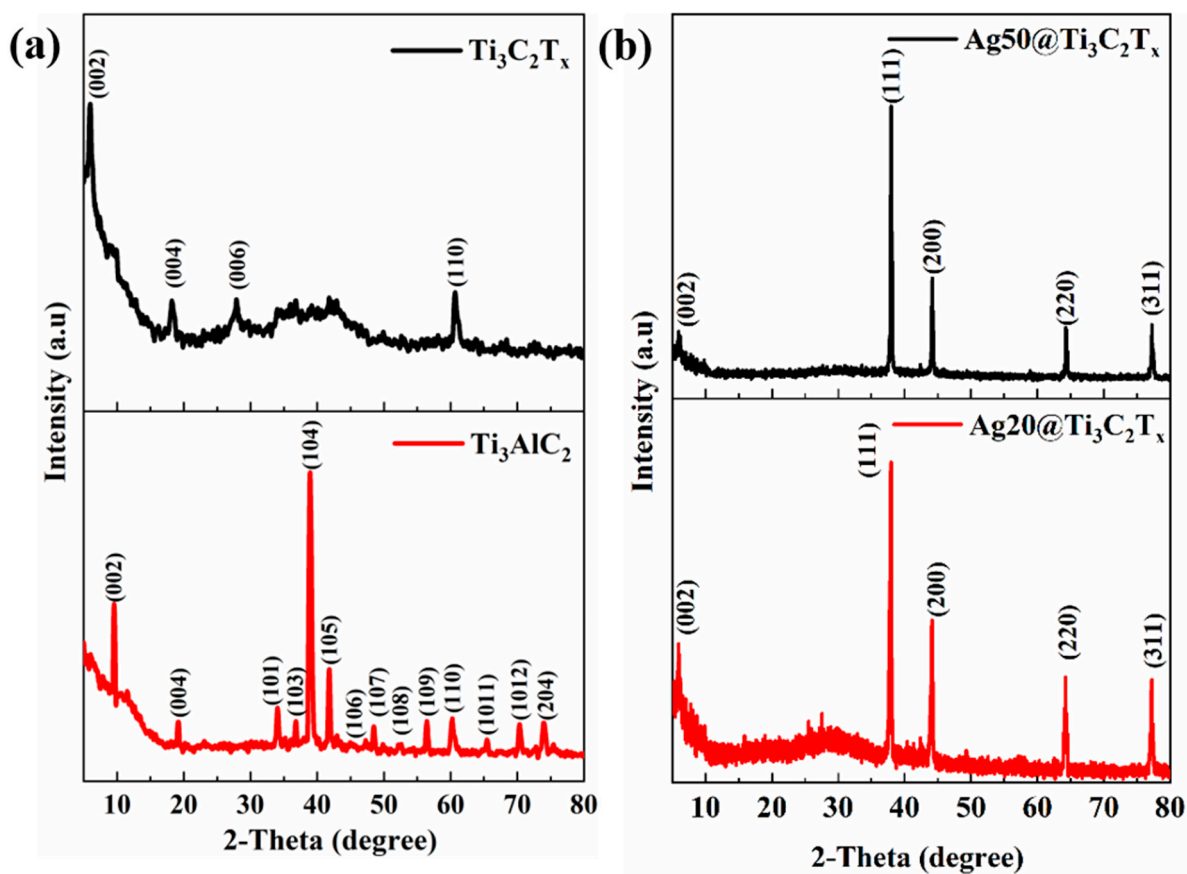


Figure 1. XRD analysis of (a) Ti_3AlC_2 , $\text{Ti}_3\text{C}_2\text{T}_x$ and (b) $\text{Ag}_{20}@\text{Ti}_3\text{C}_2\text{T}_x$, $\text{Ag}_{50}@\text{Ti}_3\text{C}_2\text{T}_x$.

The O 1s core levels showed peaks at 529.9 eV and 531.8 eV, representing the formation of C–Ti–O bonds. However, the hydroxyl terminal groups on the surface of MXene bonded to titanium atoms appeared at 531.8 eV. Finally, the hydrophilic nature of the MXene structure appeared when water molecules were inserted into the layer structure of the exfoliated structure using ultrasonication. The XPS survey spectrum of C 1s MXene-silver nanoparticles showed the signal peaks of C=C at 284.8, C–C at 285.9, and C=O at 286.8 eV [19].

The Ag 3d spectra (Figure 3b) of $\text{Ag}@\text{Ti}_3\text{C}_2\text{T}_x$ represent a double peak of Ag $3d_{5/2}$ at 365.9 eV and $3d_{3/2}$ centered at 371.9 eV, which shows the Ag reduction due to the functional groups present on the MXene surface. The absence of higher-valence Ag atoms could be confirmed by the apparent difference of ~6 eV in the binding energy of Ag 3d doublets. All Ag(0) peaks appear in the XPS survey fit using software confirming the strong reducing ability of Ti species. The mechanism of reduction of silver was similar to that of the low-valence titanium species that are responsible for the reduction of silver ions into their elemental form [11].

The surface morphology of the two-dimensional stacked layered structure of Ti_3AlC_2 , $\text{Ti}_3\text{C}_2\text{T}_x$, $\text{Ag}_{20}@\text{Ti}_3\text{C}_2\text{T}_x$, and $\text{Ag}_{50}@\text{Ti}_3\text{C}_2\text{T}_x$ are shown in Figure 4. The ternary layered structure of the MAX phase is shown in Figure 4a, while HF-etched MXene shows an accordion-like structure. Removal of aluminum from the MAX phase generates pores on the surface of the MXene sheet, which provides a platform to capture and reduce the metal nanoparticles. Silver nanoparticles are uniformly grown on the MXene sheets' surface, represented in Figure 4c,d. The average particle size of silver nanoparticles ranged from 70 to 80 nm. The elemental mapping of the MAX phase reveals the presence of C (61.17%), O (11.88%), Ti (17.54%), and Al (9.41%). After etching with HF for 40 h at 60 °C the percentage of aluminum remained only 1%, while the percentage of other elements were C, 61.18%; O, 16.07%; Ti, 13.04%; and F, 9.71%. The EDX spectrum in Figure 4e of $\text{Ag}_{50}@\text{Ti}_3\text{C}_2\text{T}_x$

shows the presence of Ag, Ti, and C elements at their respective positions, verifying the purity of samples. The elemental mapping in Figure S1 (Supporting Information) shows the homogenous distribution of elements.

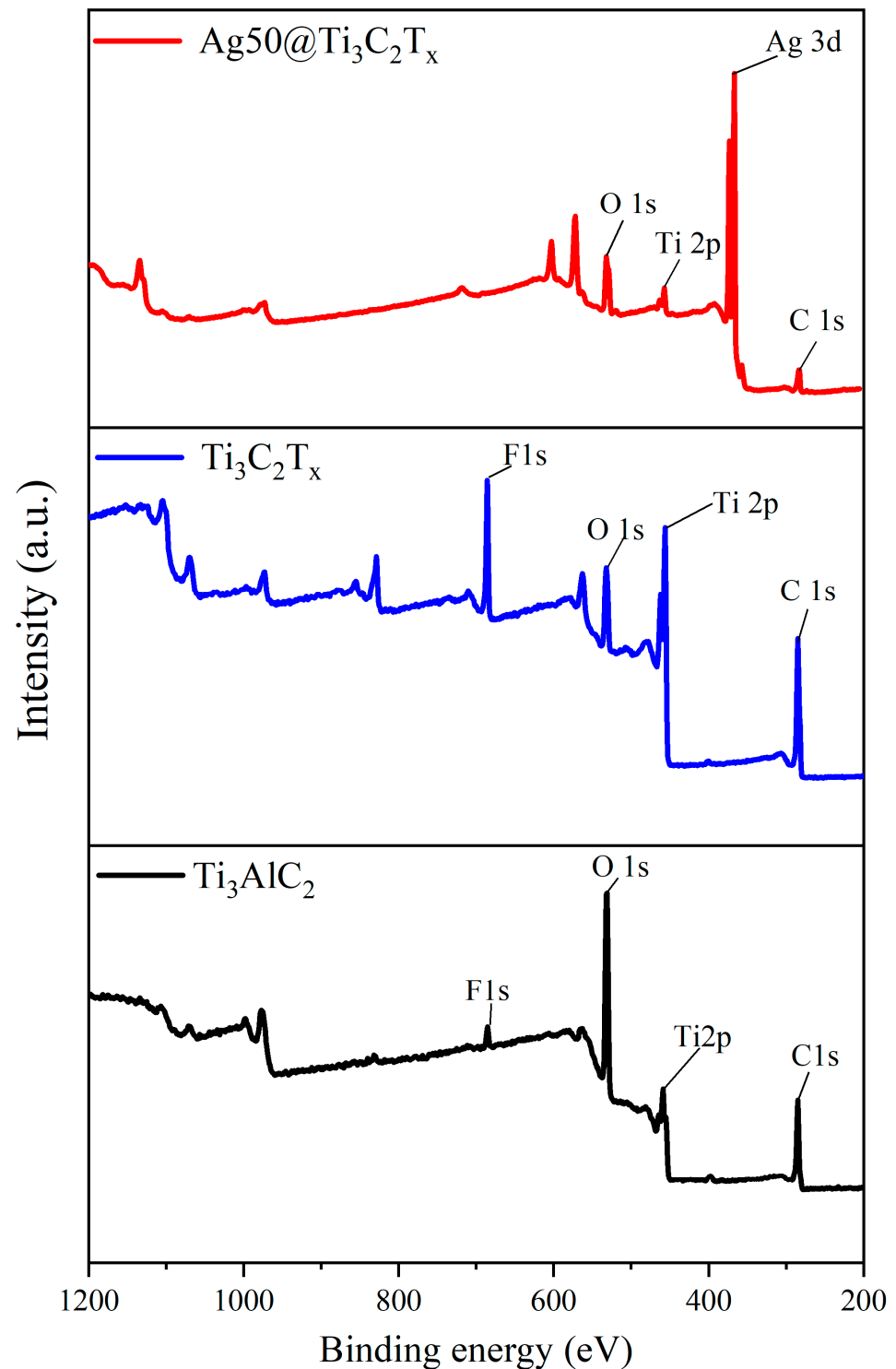


Figure 2. XPS Survey of Ti₃AlC₂, Ti₃C₂T_x, Ag50@Ti₃C₂T_x.

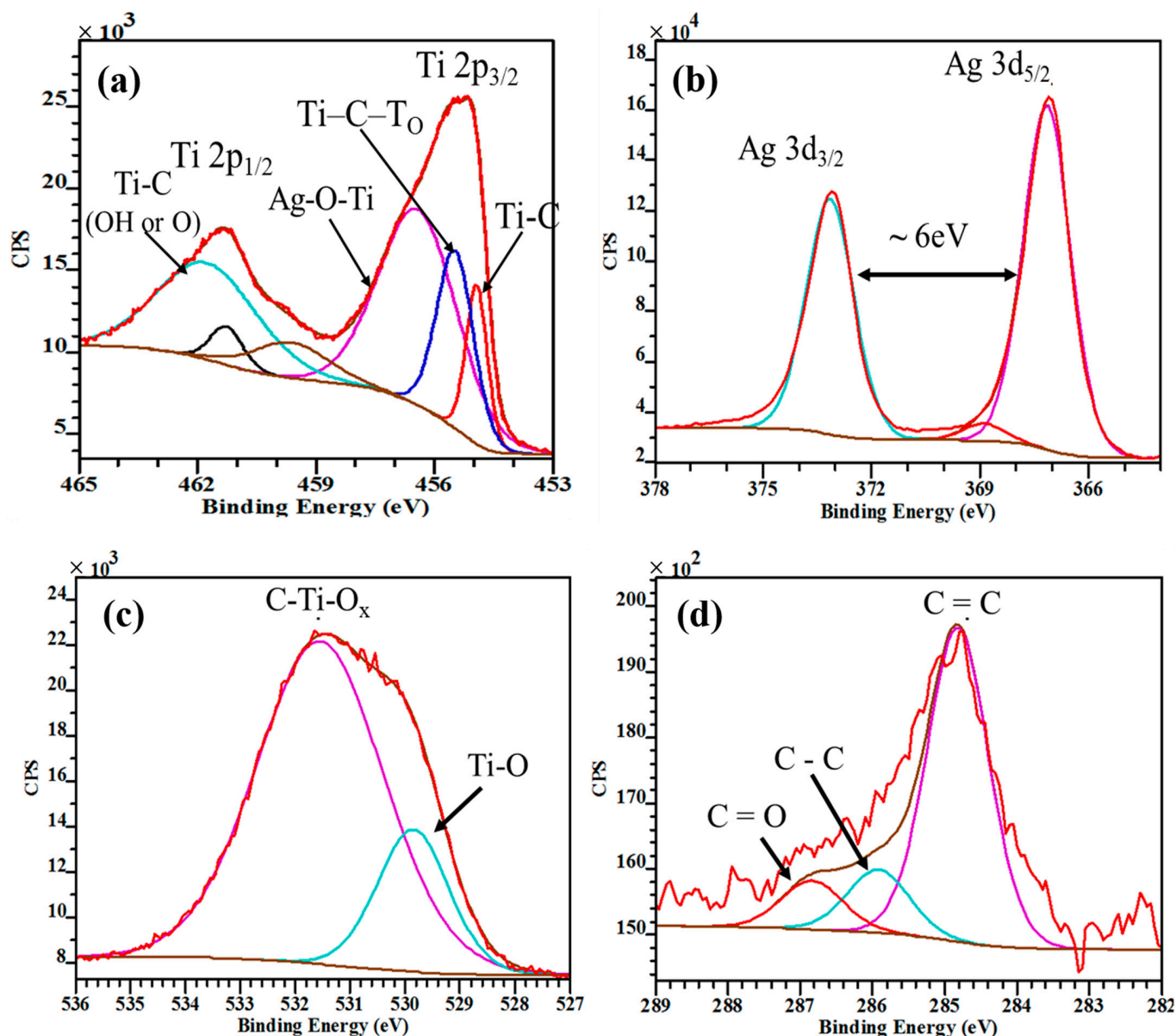


Figure 3. XPS analysis of silver-doped MXene (a) Ti 2p (b) Ag 3d (c) O 1s (d) C 1s.

The Brunauer–Emmett–Teller (BET) and Langmuir surface areas of the photocatalysts Ag20@Ti₃C₂T_x and Ag50@Ti₃C₂T_x were found to be 174.6 and 206.7 m²g^{−1}, respectively, as shown in Figure S2 (Supporting Information). Due to the uniform distribution of the silver nanoparticles on the surface of exfoliated MXene sheets, the surface area increased as compared to MXene sheets, thereby increasing the interaction of the safranin dye with the silver nanoparticles, which ultimately degraded the dye in 15 min for Ag50@Ti₃C₂T_x. The optical properties of the MXene-based Ag-nanoparticles were investigated using DRS from 1200 to 250 nm, as shown in Figure 5a. The band gap of exfoliated MXene and MXene silver nanocomposites was calculated using a Tauc plot using the following equation:

$$\alpha h\nu = A(h\nu - E_g) \quad (1)$$

where A is a constant, α is the absorbance of light, ν is the frequency of irradiated light, h is Planck's constant, and E_g is the band gap energy. The plot between $(\alpha h\nu)^2$ along the y -axis and the band gap energy on the x -axis gave the band gap of hybrid samples. Exfoliated MXene showed a band gap value of 1.24 eV; however, the value shifted to 1.35 eV after a

1:50 deposition of Ag nanoparticles, while 1:20 showed a band gap of 1.41 eV. Bare silver nanoparticles have a band gap value of 2.4 eV. This decrease in the Ag nanoparticle band gap is attributed to the incorporation of porous and stacked MXene sheets with embedded Ag nanoparticles, resulting in the intermediate state in valence and conduction bands of the MXene Ag nanocomposite along the interface, eventually causing a decrease in the band gap [16].

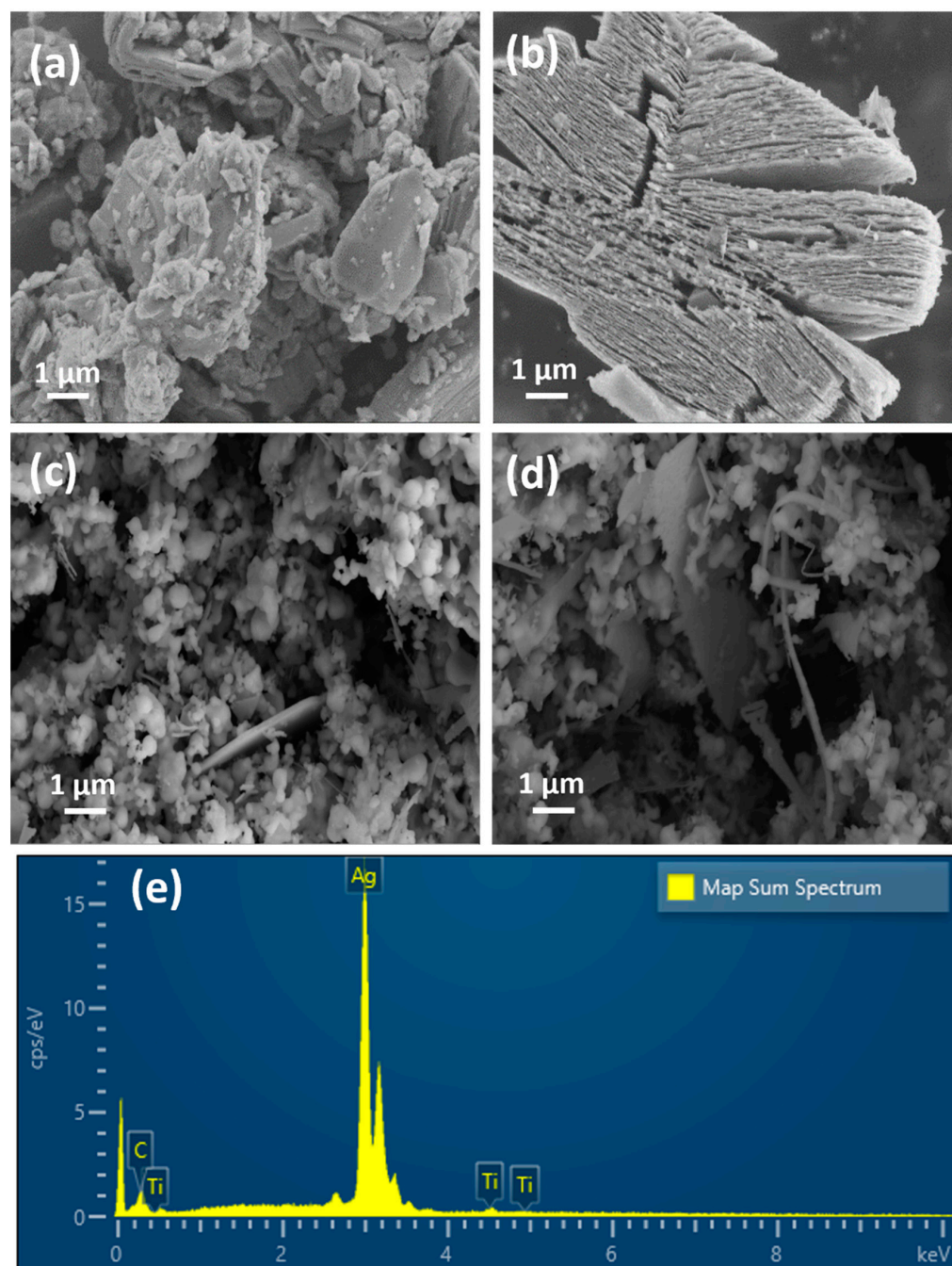


Figure 4. FESEM micrograph of (a) Ti_3AlC_2 , (b) $Ti_3C_2T_x$, (c) $Ag_{20}@Ti_3C_2T_x$, (d) $Ag_{50}@Ti_3C_2T_x$, (e) EDX spectrum of $Ag_{50}@Ti_3C_2T_x$.

The catalytic degradation activities of MXene-reduced Ag nanoparticles were investigated using safranin dye under dark and visible light conditions. In the absence of light, no degradation of safranin takes place due to the absence of electrons and holes that are generally produced in the presence of light. However, a decrease in the concentration of

dye in the dark is attributed to the adsorption–desorption phenomenon that is also taken into account. During exfoliation, negative charges are developed on the surface of $\text{Ti}_3\text{C}_2\text{T}_x$, which acts as an active site for the receptor cationic dyes. Safranin is a water-soluble cationic dye that exhibits a strong attraction with the exfoliated MXene sheets. The electron transport mechanism in the silver-doped MXene nanocomposite plays an important role in the degradation of safranin dye effectively.

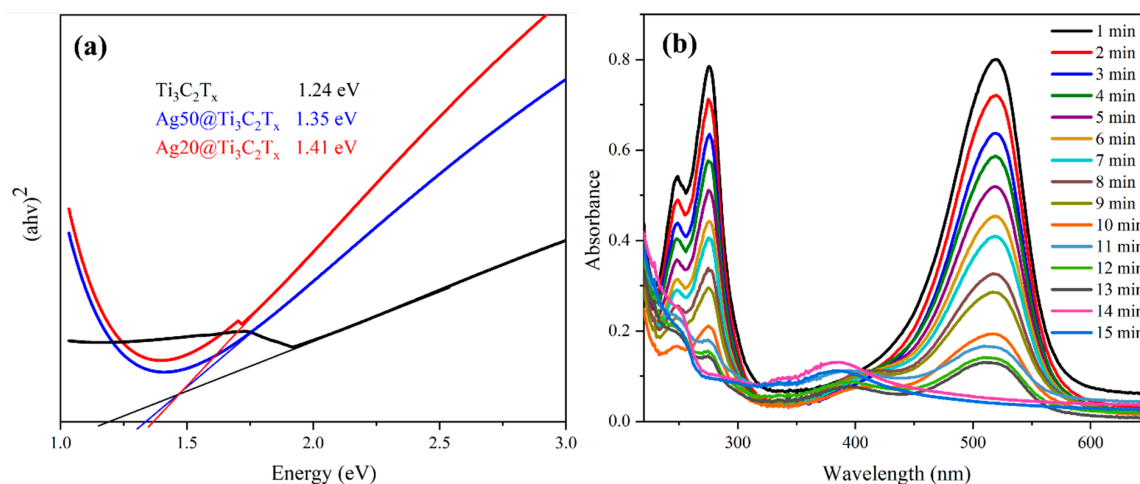


Figure 5. (a) Band gap of $\text{Ti}_3\text{C}_2\text{T}_x$, $\text{Ag20@Ti}_3\text{C}_2\text{T}_x$, $\text{Ag50@Ti}_3\text{C}_2\text{T}_x$; (b) photocatalytic degradation of safranin dye using 5 mg of $\text{Ag50@Ti}_3\text{C}_2\text{T}_x$ catalyst at different time intervals.

Visible-light-driven photocatalysis was carried out using 1, 2, and 5 mg catalyst quantities for both $\text{Ag20@Ti}_3\text{C}_2\text{T}_x$ and $\text{Ag50@Ti}_3\text{C}_2\text{T}_x$ in the range of 200–700 nm, as given in Figure 5b. The concentration of safranin dye was 30 ppm in all the degradation experiments. The catalyst was added to the dye solution and stirred for 5 min for complete interaction of dye molecules with the catalyst. Eventually, 5 mL of the suspension was centrifuged at 6000 rpm and the supernatant was analyzed under a UV–visible spectrophotometer. The decrease in the intensity at 520 nm with a peak shift to 385 nm shows the degradation of azo bonds present in the dye molecule.

The degradation efficiency of the dye is determined using the following equation:

$$\text{Degradation}(\%) = \frac{C_0 - C}{C_0} \times 100 \quad (2)$$

where ' C_0 ' is the initial concentration of dye, while ' C ' is the concentration of safranin at any time ' t '.

The reduction in the absorbance of the dye due to its adsorption on the catalyst surface in the solution is linked to the adsorption–desorption mechanism that leads to the degradation as indicated by the UV–visible spectrum. Ag nanoparticles synthesized by the addition of 50 mg MXene in $\text{Ag50@Ti}_3\text{C}_2\text{T}_x$ reduces the band gap of Ag nanoparticles, which led to the degradation of safranin dye earlier, as compared to $\text{Ag20@Ti}_3\text{C}_2\text{T}_x$. Increasing the concentration of the catalyst to 5 mg resulted in 99% degradation of the dye in 15 min, while 1 mg and 2 mg catalyst loading showed 90% and 93% degradation in 20 and 30 min, respectively, as shown in Figure 6a–c. A comparison of our study with the reported nanocomposites used for the degradation of safranin dye is given in Table 1 [32–38]. Similarly, a comparison of our study with the reported P25 commercial TiO_2 catalyst used for the degradation of safranin dye is given in Table 2 [39–42], where the prepared catalysts have performed better than the commercial TiO_2 catalyst under sunlight. To check the stability of the photocatalysts after the degradation experiments, XRD measurements were performed, and the results are shown in Figure S3 (Supporting Information). It was found

that most of the peaks due to the catalyst remained highly intact, guaranteeing the high stability of the photocatalysts.

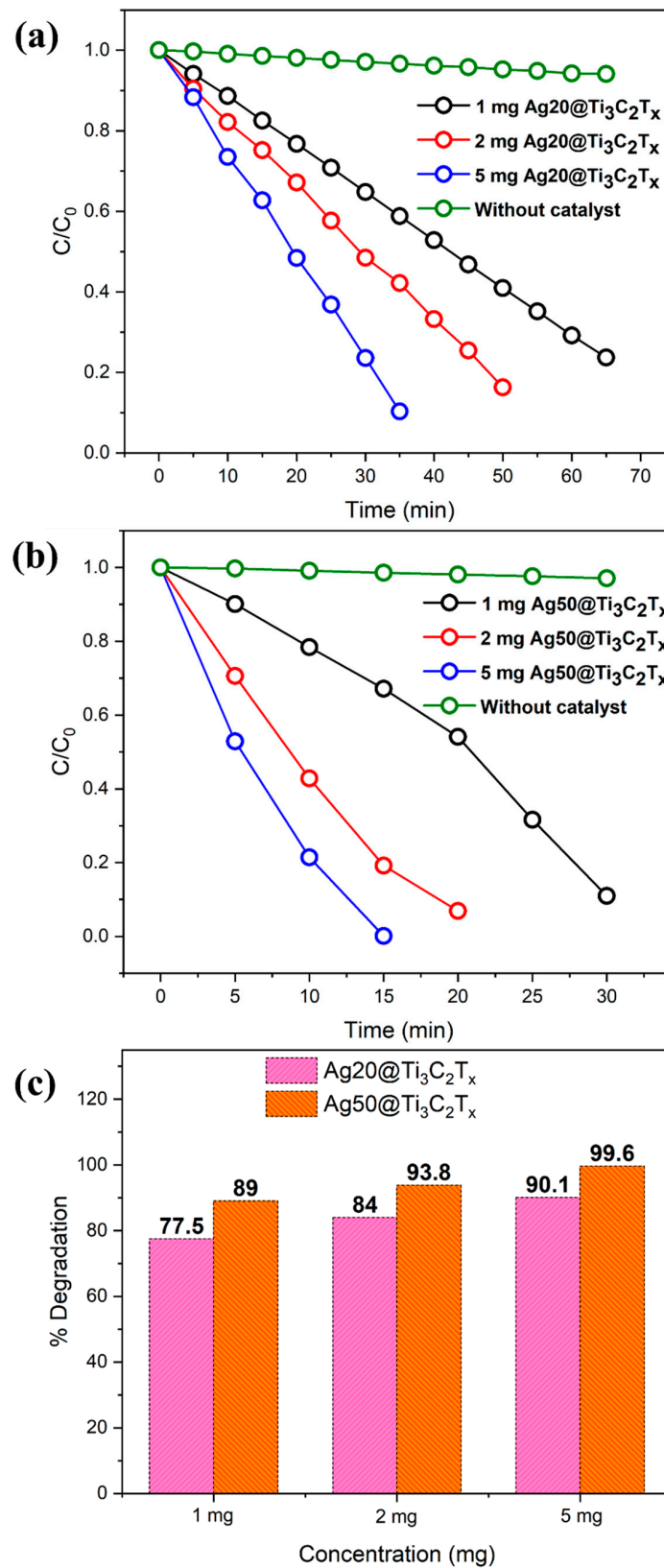


Figure 6. (a) Photocatalytic activity of Ag20@Ti₃C₂T_x and (b) Ag50@Ti₃C₂T_x; (c) percentage degradation efficiency of prepared catalysts.

Table 1. Comparison of our study with the reported nanocomposites used for the degradation of safranin dye.

Catalyst	Pollutant	Light Source	Concentration	Irradiation Time (min)	Degradation Efficiency (%)	Ref.
Ag-ZnO	Safranin T	Sunlight	2 mg	60	74.11	[32]
Ag-decorated ZnO/rGO	Safranin	Philips white LED	14 mg	80	100	[33]
FGS/ZnO nanocomposite	Safranin T	Visible light	20 mg	90	94.5	[34]
Cu nanoparticles	Safranin	UV light	25–200 g	70	95–98	[35]
LaNiSbWO ₄ -G-PANI	Safranin O	Visible light	100 mg	180	84	[36]
TiO ₂ -Bi ₂ O ₃ -CuO/ natural zeolite	Safranin O	Sunlight	80 mg	270	94.1 normal water 80.23 wastewater	[37]
Fe-ZnO	Safranin T	Sunlight	2 mg	60	99	[38]
(FGS)/ZnO nanocomposites	Safranin	Visible light	5 mg	90	94.5	[34]
Ag ₂₀ @Ti ₃ C ₂ T _x	Safranin	Visible light	5 mg	35	99.6	This study
Ag ₅₀ @Ti ₃ C ₂ T _x	Safranin	Visible light	5 mg	15	90.1	

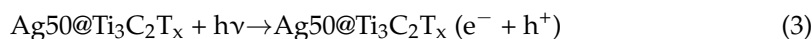
Table 2. Comparison of our study with the reported P25 commercial TiO₂ catalyst used for degradation of safranin dye.

Catalyst	Concentration	Degradation Time, Efficiency	Light Source	Reference
UV/Degussa, P25 TiO ₂	0.4 g/L	50 min, 72%	UV laser	[39]
Titanium-coated SiO ₂ NP,	89.8 mg/g	12 min, 93.29%	UV light (15W bulb of Philips)	[40]
P25 TiO ₂	100 mg	20 min, ~50.75%		
TiO ₂ (P25)	1 g/L	25 min, 100%	Simulated solar light (Xenon lamp)	[41]
WO ₃ (by ppt method)	1–8 g/L	10 min, 94%	140 mJ laser source irradiation	[42]
WO ₃ (by sol-gel)				
Degussa P-25 TiO ₂	5 mg	15 min, 99.6%	Sunlight	This study
Ag ₂₀ @Ti ₃ C ₂ T _x		35 min, 90.1%		
Ag ₅₀ @Ti ₃ C ₂ T _x				

The photocatalytic performance of the nanocomposites was determined by the degradation of safranin dye under sunlight and the recyclability tests were carried out for five successive runs for both catalyst systems. The process was performed by the separation of the photocatalyst after centrifugation at 6000 rpm, thereby washing with deionized water several times. The results are displayed in Figure S4 (Supporting Information).

Proposed Photocatalytic Mechanism

The photodegradation of safranin dye is mainly governed by the redox reactions that occur on the surface of silver nanoparticles embedded in MXene sheets in the presence of electrons and holes (Figure 7). Photogenerated electrons and holes are produced due to the interaction of visible light with the catalyst surface, which ultimately produces radical ions. The resulting radicals $\bullet\text{OH}$ and $\bullet\text{O}_2^-$ are produced where electrons reduce adsorbed O₂ molecules to form $\bullet\text{O}_2^-$, while holes oxidize water molecules into hydroxyl radicals. Being the most reactive species, these radicals interact with the dye molecules and convert them into less toxic byproducts [16]. The mechanism of safranin degradation is illustrated in the Equations (3)–(8). Equation (3) shows the visible light charge generation when light interacts with the silver-embedded MXene sheets. The layered structure of the MXene sheets traps the electrons due to their high receptive behavior and enhances the separation of charge carriers due to the large surface area of the catalyst (Equation (4)). These electrons thereby react with the adsorbed oxygen, which ultimately converts the oxides into their respective superoxide radicals, $\bullet\text{O}_2^-$; on the other hand, holes (bearing the positive charge) react with water molecules to form hydroxyl radicals, as shown in Equations (5) and (6) [16,43–45].



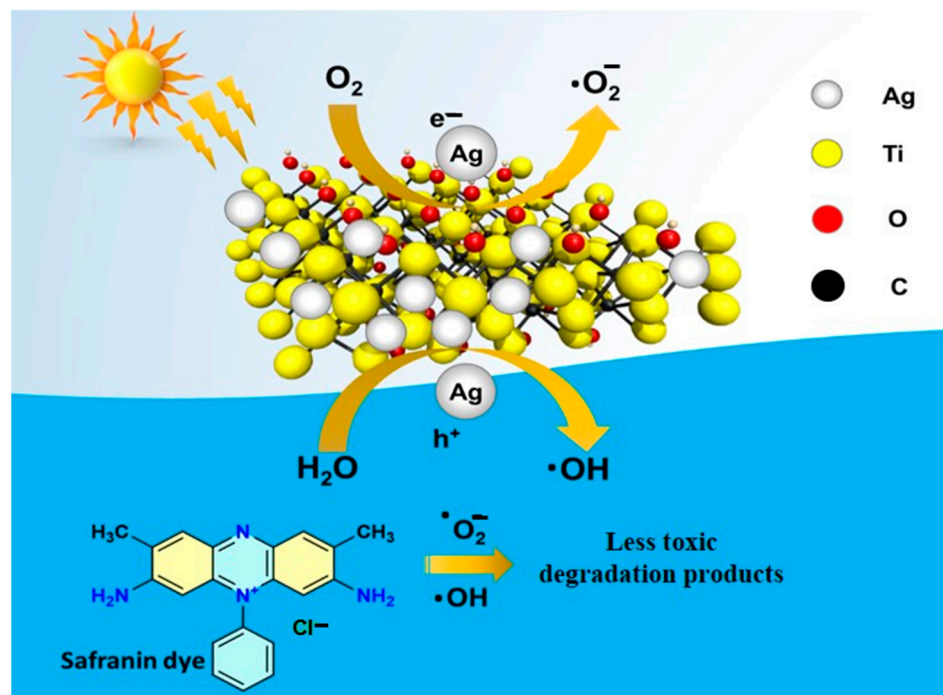
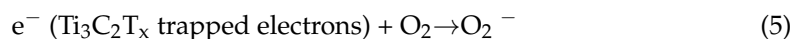


Figure 7. Proposed photocatalytic mechanism for the degradation of safranin dye using $\text{Ag}@\text{Ti}_3\text{C}_2\text{T}_x$ nanocomposite.

3. Experimental Details

3.1. Materials

Titanium aluminum carbide, (Ti_3AlC_2 , 312 MAX phase, $\geq 90\%$, particle size $\leq 40 \mu\text{m}$) was provided by Sigma-Aldrich. Silver nitrate (AgNO_3 , $\geq 99\%$) and hydrofluoric acid (HF, 48%) were purchased from Sigma-Aldrich. Polyvinyl pyrrolidone from Sigma-Aldrich was used as a dispersant. Safranin dye ($\text{C}_{20}\text{H}_{19}\text{N}_4^+\text{Cl}^-$, 99%) was provided by Merck Chemicals.

3.2. Synthesis of MXene

$\text{Ti}_3\text{C}_2\text{T}_x$ exfoliation was carried out by adding 50 mL hydrofluoric acid (48%) in a polytetrafluoroethylene conical flask with the gradual addition of 1 g Ti_3AlC_2 and the solution was continuously stirred at 60°C for 45 h. The resultant suspension of exfoliated $\text{Ti}_3\text{C}_2\text{T}_x$ sheets was centrifuged and washed with ethanol and water at 6000 rpm for 10 min until the liquid achieved a pH of ≥ 7 . To peel off the delaminated sheets, the suspension was again dissolved in water, sonicated for 2 h, and separated through vacuum filtration. After the ultrasonic treatment, the solution was centrifuged at 5000 rpm for 10 min. The resultant product obtained was vacuum dried at 60°C for 4 h.

3.3. Synthesis of MXene-Reduced Silver Nanoparticles

MXene-reduced silver nanoparticles were synthesized by sonicating 20 mg and 50 mg of hydrofluoric-acid-etched MXene in 50 mL of water separately for 30 min. After uniform dispersion, 30 mL of 0.2 M AgNO_3 in 0.2 M polyvinyl pyrrolidone was added dropwise in the above two different MXene concentrations and stirred at 60°C for 1 h. The suspension

was centrifuged at 6000 rpm and washed several times with deionized water using a vacuum filtration assembly equipped with 0.25-micron PTFE filter paper so that the pH of the solution became neutral (pH = 7). Finally, the powder was dried under vacuum at 50–60 °C for 24 h and labelled as Ag20@Ti₃C₂T_x (1:20 MXene to AgNO₃) and Ag50@Ti₃C₂T_x (1:50 MXene to AgNO₃). Figure 8 represents the schematic diagram of the procedure.

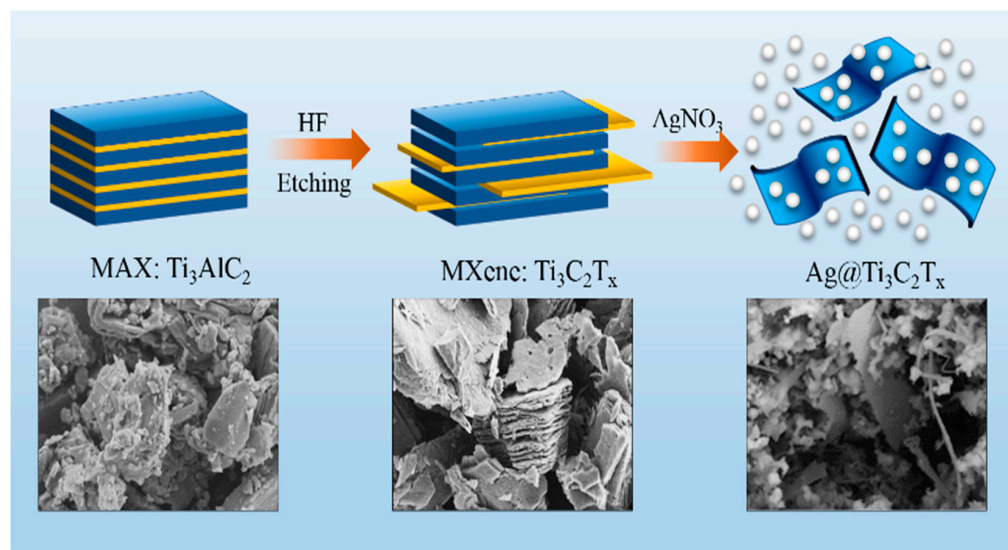


Figure 8. Schematic representation for the synthesis of Ag@Ti₃C₂T_x.

3.4. The Catalytic Activity of Ag@Ti₃C₂T_x Nanocomposite for Dye Degradation

The catalytic performance of Ag20@Ti₃C₂T_x and Ag50@Ti₃C₂T_x nanocomposites were studied using safranin dye in visible light. To investigate the degradation efficiency of the catalyst, 50 mL of freshly prepared safranin solution with an initial concentration (C_0) of 30 mg/L was used. The catalyst concentration was varied from 1 to 5 mg/L to study the impact of catalyst loading on safranin degradation. At first, the catalyst was stirred with the standard safranin solution to equilibrate the safranin solution on the surface of the nanocatalyst through the adsorption–desorption mechanism of safranin molecules at room temperature. Later, the suspension was irradiated with visible light for a specific interval of time. The degradation rate of the dye was studied using a UV–visible spectrophotometer in the range of 200–800 nm using a quartz cuvette. To test recyclability, the nanocomposite was separated by centrifuging the sample at 6000 rpm and the resultant supernatant was washed with deionized water several times.

3.5. Characterizations

The X-ray diffraction (XRD) pattern of samples was determined using a Bruker Advance D8 X-ray diffractometer, Germany, which was operated at 40 kV with a current of 40 mA and Cu K α ($\lambda = 1.54059 \text{ \AA}$) radiation source. A TESCAN MIRA (USA) field-emission scanning electron microscope (FESEM) equipped with an energy-dispersive X-ray (EDX) analyzer operated at 15 kV was used to examine the 2D structure and morphology of the samples. X-ray photoelectron spectroscopy (XPS) measurements were performed using a Scienta Omicron (Germany) equipped with a microfocused monochromatic Al K α (1486.7 eV) X-ray source with a spot size of 700 μm and an Argus analyzer. The source was operated at 15 keV with constant analyzer energy (CAE) of 100 eV for survey scans and 20 eV for high-resolution scans. The analysis of optical properties of the silver (Ag) deposited on MXene was obtained by UV–Vis DRS, Lambda 950 (USA). Catalytic efficiency was carried out by an Agilent Cary 60 UV–visible spectrophotometer (USA).

4. Conclusions

MXene-doped Ag nanocomposites (1:20 and 1:50 wt %) were synthesized by the self-reduced property of exfoliated MXene sheets using 1:20 and 1:50 wt % MXene to silver nanoparticles. The incorporation of exfoliated $Ti_3C_2T_x$ not only reduced silver salts but also decreased the band gap of silver nanoparticles from 2.5 to 1.35 eV and 1.41 eV. The decrease in band gap value is attributed to the porosity introduced by the removal of aluminum during HF etching and trapping the charged silver nanoparticles among the MXene sheets. FESEM images confirm the generation of porosity in the MXene sheets. Conducting surfaces of the MXene sheet also enable a reduction in the band gap value, which is clear from the Tauc plot. The XPS results showed that the nanohybrid materials are formed instead of simple chemical interactions. The efficiency of safranin degradation is enhanced by the addition of 5 mg of $Ag50@Ti_3C_2T_x$ (1:20 wt % MXene to silver salt) which degrades in 15 min. However, using 1 mg of the same catalyst, it takes 30 min to degrade 88% of the dye. Similarly, using $Ag20@Ti_3C_2T_x$ (1:50 wt % MXene to silver salt), ~90% of the dye degrades in 65 min. Hence, $Ag50@Ti_3C_2T_x$ shows efficient photocatalytic properties and degrades the cationic dye within 15 min using 5 mg of the catalyst, which is cost-effective and can be used for environmental remediation.

Supplementary Materials: Supplementary data to this article can be found online at <https://www.mdpi.com/article/10.3390/catal14030201/s1>, Figure S1: Elemental mapping of showing the homogenous distribution of Ag, Ti and C elements. Figure S2: BET surface area of $Ag20@Ti_3C_2T_x$ and $Ag50@Ti_3C_2T_x$. Figure S3: XRD pattern of $Ag20@Ti_3C_2T_x$ and $Ag50@Ti_3C_2T_x$ photocatalysts to check their stability after degradation experiments. Figure S4: (a) Reusability of $Ag50@Ti_3C_2T_x$ catalyst having 5 mg concentration (b) Reusability of $Ag20@Ti_3C_2T_x$ catalyst having 5 mg concentration.

Author Contributions: M.F., writing—original draft; data curation; investigation; A.R., writing—original draft; data curation; investigation; M.A. (Manawwer Alam), writing—review and editing; methodology; funding acquisition; F.W., writing—original draft; data curation; investigation; M.S., supervision; writing—review and editing; formal analysis; visualization; M.A. (Muhammad Alta), supervision; writing—review and editing; formal analysis; visualization; S.M.A., writing—review and editing; methodology; resources; validation; project administration. All authors have read and agreed to the published version of the manuscript.

Funding: The authors are thankful to the Researchers Supporting Project (RSP2024R113), King Saud University, Riyadh, Saudi Arabia.

Data Availability Statement: All data generated or analyzed during this study are included in this published article.

Conflicts of Interest: The authors declare that they have no known competing financial interests or personal relationships that could have appeared to influence the work reported in this paper.

References

1. Bai, S.; Yang, M.; Jiang, J.; He, X.; Zou, J.; Xiong, Z.; Liao, G.; Liu, S. Recent advances of MXenes as electrocatalysts for hydrogen evolution reaction. *NPJ 2D Mater. Appl.* **2021**, *5*, 78. [CrossRef]
2. Natu, V.; Pai, R.; Sokol, M.; Carey, M.; Kalra, V.; Barsoum, M.W. 2D $Ti_3C_2T_z$ MXene synthesized by water-free etching of Ti_3AlC_2 in polar organic solvents. *Chem* **2020**, *6*, 616–630. [CrossRef]
3. Anasori, B.; Lukatskaya, M.R.; Gogotsi, Y. 2D metal carbides and nitrides (MXenes) for energy storage. *Nat. Rev. Mater.* **2017**, *2*, 16098. [CrossRef]
4. Tasleem, S.; Tahir, M.; Zakaria, Z.Y. Fabricating structured 2D Ti_3AlC_2 MAX dispersed TiO_2 heterostructure with Ni_2P as a cocatalyst for efficient photocatalytic H_2 production. *J. Alloys Compd.* **2020**, *842*, 155752. [CrossRef]
5. Husmann, S.; Budak, Ö.; Shim, H.; Liang, K.; Aslan, M.; Kruth, A.; Quade, A.; Naguib, M.; Presser, V. Ionic liquid-based synthesis of MXene. *Chem. Commun.* **2020**, *56*, 11082–11085. [CrossRef]
6. Zhao, J.; Zhang, L.; Xie, X.-Y.; Li, X.; Ma, Y.; Liu, Q.; Fang, W.-H.; Shi, X.; Cui, G.; Sun, X. $Ti_3C_2T_x$ (T = F, OH) MXene nanosheets: Conductive 2D catalysts for ambient electrohydrogenation of N_2 to NH_3 . *J. Mater. Chem. A* **2018**, *6*, 24031–24035. [CrossRef]
7. Feng, X.; Yu, Z.; Sun, Y.; Long, R.; Shan, M.; Li, X.; Liu, Y.; Liu, J. Review MXenes as a new type of nanomaterial for environmental applications in the photocatalytic degradation of water pollutants. *Ceram. Int.* **2021**, *47*, 7321–7343. [CrossRef]
8. Wang, K.; Li, Y.; Li, J.; Zhang, G. Boosting interfacial charge separation of $Ba_5Nb_4O_{15}/g-C_3N_4$ photocatalysts by 2D/2D nanojunction towards efficient visible-light driven H_2 generation. *Appl. Catal. B Environ.* **2020**, *263*, 117730. [CrossRef]

9. Jiang, L.; Li, J.; Wang, K.; Zhang, G.; Li, Y.; Wu, X. Low boiling point solvent mediated strategy to synthesize functionalized monolayer carbon nitride for superior photocatalytic hydrogen evolution. *Appl. Catal. B Environ.* **2020**, *260*, 118181. [[CrossRef](#)]
10. Sun, Y.; Li, Y. Potential environmental applications of MXenes: A critical review. *Chemosphere* **2021**, *271*, 129578. [[CrossRef](#)]
11. Tunesi, M.M.; Soomro, R.A.; Han, X.; Zhu, Q.; Wei, Y.; Xu, B. Application of MXenes in environmental remediation technologies. *Nano Converg.* **2021**, *8*, 5. [[CrossRef](#)]
12. Jiang, X.; Kuklin, A.V.; Baev, A.; Ge, Y.; Ågren, H.; Zhang, H.; Prasad, P.N. Two-dimensional MXenes: From morphological to optical, electric, and magnetic properties and applications. *Phys. Rep.* **2020**, *848*, 1–58. [[CrossRef](#)]
13. Im, J.K.; Sohn, E.J.; Kim, S.; Jang, M.; Son, A.; Zoh, K.-D.; Yoon, Y. Review of MXene-based nanocomposites for photocatalysis. *Chemosphere* **2021**, *270*, 129478. [[CrossRef](#)]
14. Othman, Z.; Sinopoli, A.; Mackey, H.R.; Mahmoud, K.A. Efficient Photocatalytic Degradation of Organic Dyes by AgNPs/TiO₂/Ti₃C₂T_x MXene Composites under UV and Solar Light. *ACS Omega* **2021**, *6*, 33325–33338. [[CrossRef](#)]
15. Luo, S.; Wang, R.; Yin, J.; Jiao, T.; Chen, K.; Zou, G.; Zhang, L.; Zhou, J.; Zhang, L.; Peng, Q. Preparation and dye degradation performances of self-assembled MXene-Co₃O₄ nanocomposites synthesized via solvothermal approach. *ACS Omega* **2019**, *4*, 3946–3953. [[CrossRef](#)]
16. Tariq, A.; Ali, S.I.; Akinwande, D.; Rizwan, S. Efficient visible-light photocatalysis of 2D-MXene nanohybrids with Gd³⁺-and Sn⁴⁺-codoped bismuth ferrite. *ACS Omega* **2018**, *3*, 13828–13836. [[CrossRef](#)]
17. Li, Y.; Yin, Z.; Ji, G.; Liang, Z.; Xue, Y.; Guo, Y.; Tian, J.; Wang, X.; Cui, H. 2D/2D/2D heterojunction of Ti₃C₂ MXene/MoS₂ nanosheets/TiO₂ nanosheets with exposed (001) facets toward enhanced photocatalytic hydrogen production activity. *Appl. Catal. B Environ.* **2019**, *246*, 12–20. [[CrossRef](#)]
18. Tie, L.; Yang, S.; Yu, C.; Chen, H.; Liu, Y.; Dong, S.; Sun, J.; Sun, J. In situ decoration of ZnS nanoparticles with Ti₃C₂ MXene nanosheets for efficient photocatalytic hydrogen evolution. *J. Colloid Interface Sci.* **2019**, *545*, 63–70. [[CrossRef](#)]
19. Low, J.; Zhang, L.; Tong, T.; Shen, B.; Yu, J. TiO₂/MXene Ti₃C₂ composite with excellent photocatalytic CO₂ reduction activity. *J. Catal.* **2018**, *361*, 255–266. [[CrossRef](#)]
20. Liu, Q.; Ai, L.; Jiang, J. MXene-derived TiO₂@C/gC₃N₄ heterojunctions for highly efficient nitrogen photofixation. *J. Mater. Chem. A* **2018**, *6*, 4102–4110. [[CrossRef](#)]
21. Cao, Y.; Fang, Y.; Lei, X.; Tan, B.; Hu, X.; Liu, B.; Chen, Q. Fabrication of novel CuFe₂O₄/MXene hierarchical heterostructures for enhanced photocatalytic degradation of sulfonamides under visible light. *J. Hazard. Mater.* **2020**, *387*, 122021. [[CrossRef](#)]
22. Fang, H.; Pan, Y.; Yan, H.; Qin, X.; Wang, C.; Xu, L.; Pan, C. Facile preparation of Yb³⁺/Tm³⁺ co-doped Ti₃C₂/Ag/Ag₃VO₄ composite with an efficient charge separation for boosting visible-light photocatalytic activity. *Appl. Surf. Sci.* **2020**, *527*, 146909. [[CrossRef](#)]
23. Wang, Z.; Wang, K.; Li, Y.; Jiang, L.; Zhang, G. Novel BiSbO₄/BiOBr nanoarchitecture with enhanced visible-light driven photocatalytic performance: Oxygen-induced pathway of activation and mechanism unveiling. *Appl. Surf. Sci.* **2019**, *498*, 143850. [[CrossRef](#)]
24. Wu, Y.; Li, X.; Yang, Q.; Wang, D.; Yao, F.; Cao, J.; Chen, Z.; Huang, X.; Yang, Y.; Li, X. Mxene-modulated dual-heterojunction generation on a metal-organic framework (MOF) via surface constitution reconstruction for enhanced photocatalytic activity. *Chem. Eng. J.* **2020**, *390*, 124519. [[CrossRef](#)]
25. Li, Z.K.; Wei, Y.; Gao, X.; Ding, L.; Lu, Z.; Deng, J.; Yang, X.; Caro, J.; Wang, H. Antibiotics separation with MXene membranes based on regularly stacked high-aspect-ratio nanosheets. *Angew. Chem. Int. Ed.* **2020**, *59*, 9751–9756. [[CrossRef](#)]
26. Liu, Y.; Luo, R.; Li, Y.; Qi, J.; Wang, C.; Li, J.; Sun, X.; Wang, L. Sandwich-like Co₃O₄/MXene composite with enhanced catalytic performance for Bisphenol A degradation. *Chem. Eng. J.* **2018**, *347*, 731–740. [[CrossRef](#)]
27. Iravani, S.; Varma, R.S. MXene-based photocatalysts in degradation of organic and pharmaceutical pollutants. *Molecules* **2022**, *27*, 6939. [[CrossRef](#)]
28. Lorencova, L.; Gajdosova, V.; Hroncekova, S.; Bertok, T.; Jerigova, M.; Velic, D.; Sobolciak, P.; Krupa, I.; Kasak, P.; Tkac, J. Electrochemical Investigation of Interfacial Properties of Ti₃C₂T_x MXene Modified by Aryldiazonium Betaine Derivatives. *Front. Chem.* **2020**, *8*, 553. [[CrossRef](#)]
29. Zhu, X.; Zhu, Y.; Jia, K.; Abraha, B.S.; Li, Y.; Peng, W.; Zhang, F.; Fan, X.; Zhang, L. A near-infrared light-mediated antimicrobial based on Ag/Ti₃C₂T_x for effective synergetic antibacterial applications. *Nanoscale* **2020**, *12*, 19129–19141. [[CrossRef](#)]
30. Na, L.-Å.; Persson, P.O.; Rosen, J. X-ray Photoelectron Spectroscopy of Ti₃AlC₂, Ti₃C₂T_z, and TiC Provides Evidence for the Electrostatic Interaction between Laminated Layers in MAX-Phase Materials. *J. Phys. Chem. C* **2020**, *124*, 27732–27742.
31. Lv, Y.; Wang, K.; Li, D.; Li, P.; Chen, X.; Han, W. Rare Ag nanoparticles loading induced surface-enhanced pollutant adsorption and photocatalytic degradation on Ti₃C₂T_x MXene-based nanosheets. *Chem. Phys.* **2022**, *560*, 111591. [[CrossRef](#)]
32. Ahmad, K.S.; Jaffri, S.B. Phytosynthetic Ag doped ZnO nanoparticles: Semiconducting green remediators: Photocatalytic and antimicrobial potential of green nanoparticles. *Open Chem.* **2018**, *16*, 556–570. [[CrossRef](#)]
33. Saraffin, R.S.; Kapuria, A.; Saha, S.K.; Dutta, K. Eco-friendly hetero-system silver decorated nanocomposite zinc oxide/reduced graphene oxide: Improved broad-ranged absorptivity and enhanced photocatalytic performance under white-light irradiation. *React. Kinet. Mech. Catal.* **2022**, *135*, 2827–2850. [[CrossRef](#)]
34. Nenavathu, B.P.; Kandula, S.; Verma, S. Visible-light-driven photocatalytic degradation of safranin-T dye using functionalized graphene oxide nanosheet (FGS)/ZnO nanocomposites. *RSC Adv.* **2018**, *8*, 19659–19667. [[CrossRef](#)]

35. El-Berry, M.F.; Sadeek, S.A.; Abdalla, A.M.; Nassar, M.Y. Microwave-assisted fabrication of copper nanoparticles utilizing different counter ions: An efficient photocatalyst for photocatalytic degradation of safranin dye from aqueous media. *Mater. Res. Bull.* **2021**, *133*, 111048. [[CrossRef](#)]
36. Oh, W.-C.; Fatema, K.N.; Liu, Y.; Lim, C.S.; Cho, K.Y.; Jung, C.-H.; Biswas, M.R.U.D. Sonochemical synthesis of quaternary LaNiSbWO₄-G-PANI polymer nanocomposite for photocatalytic degradation of Safranin-O and gallic acid under visible light irradiation. *J. Photochem. Photobiol. A Chem.* **2020**, *394*, 112484. [[CrossRef](#)]
37. Boudraa, R.; Talantikite-Touati, D.; Souici, A.; Djermoune, A.; Saidani, A.; Fendi, K.; Amrane, A.; Bollinger, J.-C.; Tran, H.N.; Hadadi, A. Optical and photocatalytic properties of TiO₂-Bi₂O₃-CuO supported on natural zeolite for removing Safranin-O dye from water and wastewater. *J. Photochem. Photobiol. A Chem.* **2023**, *443*, 114845. [[CrossRef](#)]
38. Sadiq, M.U.; Shah, A.; Nisar, J.; Shah, I. Photoelectrocatalytic Detection and Degradation Studies of a Hazardous Textile Dye Safranin T. *Nanomaterials* **2023**, *13*, 2218. [[CrossRef](#)]
39. Bendjama, M.; Hamdaoui, O.; Ferkous, H.; Alghyamah, A. Degradation of Safranin O in Water by UV/TiO₂/IO₄⁻ Process: Effect of Operating Conditions and Mineralization. *Catalysts* **2022**, *12*, 1460. [[CrossRef](#)]
40. Ekka, B.; Sahu, M.K.; Patel, R.K.; Dash, P. Titania coated silica nanocomposite prepared via encapsulation method for the degradation of Safranin-O dye from aqueous solution: Optimization using statistical design. *Water Resour. Ind.* **2019**, *22*, 100071. [[CrossRef](#)]
41. Ge, M.; Hu, Z.; Wei, J.; He, Q.; He, Z. Recent advances in persulfate-assisted TiO₂-based photocatalysis for wastewater treatment: Performances, mechanism and perspectives. *J. Alloys Compd.* **2021**, *888*, 161625. [[CrossRef](#)]
42. Hayat, K.; Gondal, M.; Khaled, M.; Yamani, Z.; Ahmed, S. Laser induced photocatalytic degradation of hazardous dye (Safranin-O) using self synthesized nanocrystalline WO₃. *J. Hazard. Mater.* **2011**, *186*, 1226–1233. [[CrossRef](#)] [[PubMed](#)]
43. Iqbal, M.A.; Ali, S.I.; Amin, F.; Tariq, A.; Iqbal, M.Z.; Rizwan, S. La- and Mn-codoped Bismuth Ferrite/Ti₃C₂ MXene composites for efficient photocatalytic degradation of Congo Red dye. *ACS Omega* **2019**, *4*, 8661–8668. [[CrossRef](#)] [[PubMed](#)]
44. Irfan, S.; Shen, Y.; Rizwan, S.; Wang, H.C.; Khan, S.B.; Nan, C.W. Band-gap engineering and enhanced photocatalytic activity of Sm and Mn doped BiFeO₃ nanoparticles. *J. Am. Ceram. Soc.* **2017**, *100*, 31–40. [[CrossRef](#)]
45. Li, X.; Yu, J.; Jaroniec, M.; Chen, X. Cocatalysts for selective photoreduction of CO₂ into solar fuels. *Chem. Rev.* **2019**, *119*, 3962–4179. [[CrossRef](#)]

Disclaimer/Publisher's Note: The statements, opinions and data contained in all publications are solely those of the individual author(s) and contributor(s) and not of MDPI and/or the editor(s). MDPI and/or the editor(s) disclaim responsibility for any injury to people or property resulting from any ideas, methods, instructions or products referred to in the content.